Periplasm homeostatic regulation maintains spatial constraints essential for cell envelope processes and cell viability.

Eric Mandela[1,+], Christopher J. Stubenrauch[1,+], David Ryoo[2], Hyea Hwang[3,#], Eli J. Cohen[4], Von L. Torres[1], Pankaj Deo[1], Chaille T. Webb[1], Cheng Huang[5], Ralf B. Schittenhelm[5], Morgan Beeby[4], JC Gumbart[6,*], Trevor Lithgow[1,*] & Iain D. Hay[7,*]

1 - Infection & Immunity Program, Biomedicine Discovery Institute and Department of Microbiology, Monash University, Clayton, 3800, Australia

2 - Interdisciplinary Bioengineering Graduate Program, Georgia Institute of Technology, Atlanta, GA 30332, USA

3 - School of Materials Science and Engineering, Georgia Institute of Technology, Atlanta, Georgia 30332-0430, USA

4 - Department of Life Sciences, Imperial College London, London SW7 2AZ, UK.

5 - Monash Proteomics & Metabolomics Facility, Department of Biochemistry and Molecular Biology, Biomedicine Discovery Institute, Monash University, Clayton, 3800, Australia

6 - School of Physics, Georgia Institute of Technology, Atlanta, Georgia 30332-0430, USA

7 - School of Biological Sciences, The University of Auckland, Auckland 1010, New Zealand

- Present address: NIH Center for Macromolecular Modeling and Bioinformatics, Beckman Institute for Advanced Science and Technology, Department of Biochemistry, Center for Biophysics and Quantitative Biology, University of Illinois at Urbana-Champaign, Urbana, IL, USA

+ - These authors contributed equally

* - To whom correspondence should be addressed: iain.hay@auckland.ac.nz, trevor.lithgow@monash.edu, jcgumbart@gatech.edu

ABSTRACT

The cell envelope of Gram-negative bacteria consists of two membranes surrounding a periplasm and peptidoglycan layer. Molecular machines spanning the cell envelope depend on spatial constraints and load-bearing forces across the cell envelope and surface. The mechanisms dictating spatial constraints across the cell envelope remain incompletely defined. In *Escherichia coli*, the coiled-coil lipoprotein Lpp contributes the only covalent linkage between the outer membrane and the underlying peptidoglycan layer. Using proteomics, molecular dynamics and a synthetic lethal screen we show that lengthening Lpp to the upper limit does not change the spatial constraint, but rather impacts the load-bearing capacity across the outer membrane. Our findings demonstrate *E. coli* expressing elongated Lpp homeostatically counteracts periplasmic enlargement with a combination of tilting Lpp and reducing Lpp abundance. By genetic screening we identified all of the genes in *E. coli* that become essential in order to enact this homeostasis, and by quantitative proteomics discovered that very few proteins need to be up- or down-regulated in steady-state levels in order to enact this homeostasis. We observed increased levels of factors determining cell stiffness, decrease membrane integrity, increase membrane vesiculation and a dependance on otherwise non-essential tethers to maintain lipid transport and peptidoglycan biosynthesis. Further this has implications for understanding how spatial constraint across the envelope controls processes such as flagellum-driven motility, cellular signaling and protein translocation

42 **INTRODUCTION**

43

44 Gram-negative bacteria have a cell envelope composed of two membranes sandwiching between them an
45 aqueous space called the periplasm, in which an essential structural layer of peptidoglycan (PG) resides. The
46 outer membrane is critical to cell growth and these bacteria face challenges to their cell biology in terms of
47 membrane protein assembly and lipid-transport pathways that must traverse the distance from the inner
48 membrane (IM) to the outer membrane (OM) [1]. Recent work investigating the spatial demands for assembly
49 of proteins into the outer membrane has shown precincts of active protein integration into the membrane can
50 deliver new material to the growing outer membrane [2] and that random planar movement from these precincts
51 drives the observed non-uniform distributions of the major proteins of the outer membrane [3, 4]. By contrast to
52 these protein components that diffuse to the outer membrane, elements of the LPS-transport machinery (eg.
53 the Lpt complex) [5, 6, 7, 8, 9] span the OM and IM in order to fulfil their function in delivering lipid components
54 to the outer membrane.

55

56 The PG layer is a fundamental aspect of the cell envelope, and it must be dynamically remodeled to allow
57 growth as well as the assembly and transit of trans-envelope structures. PG synthesis and remodeling is a
58 complex process with high levels of redundancy at various steps, involving at least 50 enzymes in *E. coli* [10].
59 The Penicillin-binding proteins (PBPs) are the core components responsible for the periplasmic biosynthesis
60 of peptidoglycan. There are multiple PBP complexes including the two core, semi-redundant PBP complexes
61 PBP1a and PBP1b embedded in the IM which are activated by interactions with lipoproteins LpoA and LpoB
62 embedded in the OM. Thus the activation of PG synthesis by these enzymes is spatially regulated, serving as
63 a self-limiting molecular ruler to modulate PG thickness [11]. Cells must possess either a functional PBP1a or
64 PBP1b system for growth [12, 13].

65

66 Trans-envelope complexes such as lipopolysaccharide (LPS) transit pathways [5, 6, 7, 8, 9] and the protein
67 translocation and assembly module (the TAM) [14, 15, 16] are also spatially constrained by the need to reach across
68 from the IM to OM in order to function. The PG layer is covalently attached to the outer membrane by Braun's
69 lipoprotein (Lpp), with two recent papers addressing whether extending the length of Lpp would impact on (i)
70 flagellar function given that the flagellum spans both membranes [17], and (ii) signal-transduction systems that
71 span the OM to IM [18]. In both cases, extending the coiled-coil structure of Lpp by 21 residues (Lpp^{+21}) was
72 found to be the longest form that supported close to normal growth [17, 18]. Imaging of these Lpp^{+21} strains in
73 both studies showed that the total periplasmic width had been stretched ~3-4 nm [17, 18]. This being the case, the
74 Lpp^{+21} model would provide a powerful experimental system to study how processes like OM biogenesis and
75 PG biosynthesis can be maintained under a spatial stress on the cell wall.

76

77 To understand how trans-envelope processes in *E. coli* adapt to the presence of an enlarged periplasm, a
78 combination of phenotypic analysis, proteomics, molecular dynamics and a synthetic lethal screen was
79 employed to identify and characterize factors needed to maintain viability in the Lpp^{+21} strain of *E. coli*. The
80 genetic screen demanded synthetic growth phenotypes from an array of mutants each lacking a gene that,
81 while non-essential in wild-type *E. coli* [19], is essential in the Lpp^{+21} strain. These genes fall into three functional
82 categories: PG biosynthesis and remodelling, LPS biosynthesis and PG-outer membrane linkage. We show
83 that previously non-essential proteins involved in bridging the gap between the OM and PG become essential
84 in the context of the Lpp^{+21} strain background. These include previously known PG binding OM proteins
85 (OmpA and Pal) as well as proteins previously not known to play an active role in linking the OM and PG
86 (TolC and YiaD). We observed a thicker more diffuse or heterogeneous PG layer in the Lpp^{+21} strain and
87 whole cell proteomics revealed that in response to an increased length of Lpp, *E. coli* increases the levels of a
88 range of cell envelope proteins involved in PG turnover. We discuss the outcomes in terms of how the PG-
89 outer membrane linkage functionalizes the periplasm, the evolutionary constrains in place to maintain this
90 functionality, and the specific activity of Lpp in contributing to the load-bearing function of the OM.
91

92 **RESULTS**

93

94 ***Resilience and growth of the Lpp^{+21} strain***

95 A phylogenetic assessment of Lpp lengths across diverse bacterial lineages showed a very narrow window of
96 protein size (Fig. 1A), with Lpp being 78 residues in most species of bacteria including *E. coli*. Lpp lengths
97 of 99 residues or more are at the upper end of the natural range for this protein and, in nature, these longer
98 Lpp proteins are found in the genus *Geobacter*. The previously described Lpp^{+21} isoform expressed in *E. coli*
99 therefore sits near the upper physiological range observed among bacteria. We introduced a gene encoding
100 the Lpp^{+21} isoform into an *E. coli* background suitable for genetic screens (Fig. S1) and confirmed the size of
101 the protein by SDS-PAGE of bacterial cell extracts (Fig. 1B). Enteric bacteria like *E. coli* can thrive in
102 hyperosmotic environments compared to most laboratory growth media, such as the human gut by maintaining
103 the periplasm and the cytoplasm in an iso-osmotic state [20, 21]. This is achieved by adjusting the solute
104 concentration in the cell compartments by influx or efflux of water. By doing so, osmolality contributes
105 immensely to the architectural aspects of cellular compartments [21, 22]. In this study sorbitol was used to mimic
106 these physiological osmotic conditions. Previous studies have demonstrated that the periplasmic volume
107 increased rapidly in response to increased osmolyte levels in the external medium. This phenomenon can
108 reduce the cytoplasmic volume by about 30%, thereby constricting the IM inwards, and substantially
109 increasing the periplasmic volume by around 300% [21, 22, 23]. The Lpp^{+21} isoform had little impact on growth of
110 *E. coli*. On minimal growth medium, growth rates of the Lpp^{+21} strain of *E. coli* were equivalent to the isogenic
111 wild-type *E. coli* (Fig. 1C). This was likewise true on growth media osmotically balanced with concentrations
112 of sorbitol up to 1.0M (Fig. 1D), and on rich (LB) medium with or without sorbitol (Fig. 1D).

113

114 To establish the extent to which the periplasm had been remodeled in the Lpp^{+21} strain of *E. coli*, we compared
115 the periplasms of WT and Lpp^{+21} strains using electron cryotomography in which cells are preserved in a
116 frozen-hydrated, near-native state. To discern peptidoglycan, which was indistinct in previous studies, we
117 increased the signal to noise ratio in images by calculating subtomogram averages instead of inspecting
118 individual tomograms. As expected, the average distance from the middle of the IM density to the middle of
119 the OM density was increased in both strains under hyperosmotic conditions when compared to previously
120 reported data where cells were grown in standard laboratory media [18]. As shown in Fig. 1E, the averaged
121 distance from the IM to the OM were somewhat greater in the Lpp^{+21} strain (32-36nm) compared to the
122 isogenic wild-type strain (30-32nm) in line with previous Lpp+21 periplasmic width measurements. Previous
123 studies could not discern peptidoglycan; whereas here, we were able discern peptidoglycan in subtomogram
124 averages. The distance to the center of the PG density from the OM was slightly increased in the Lpp^{+21} strain
125 (Fig. 1F), although by less than the anticipated ~3 nm. The PG morphology was also qualitatively different:
126 in the wild-type strain a uniform dark PG layer could be observed in the images, whereas in the Lpp^{+21} strain

a broader and more diffuse PG layer was evident, suggesting heterogeneity in both the density and thickness of the PG.

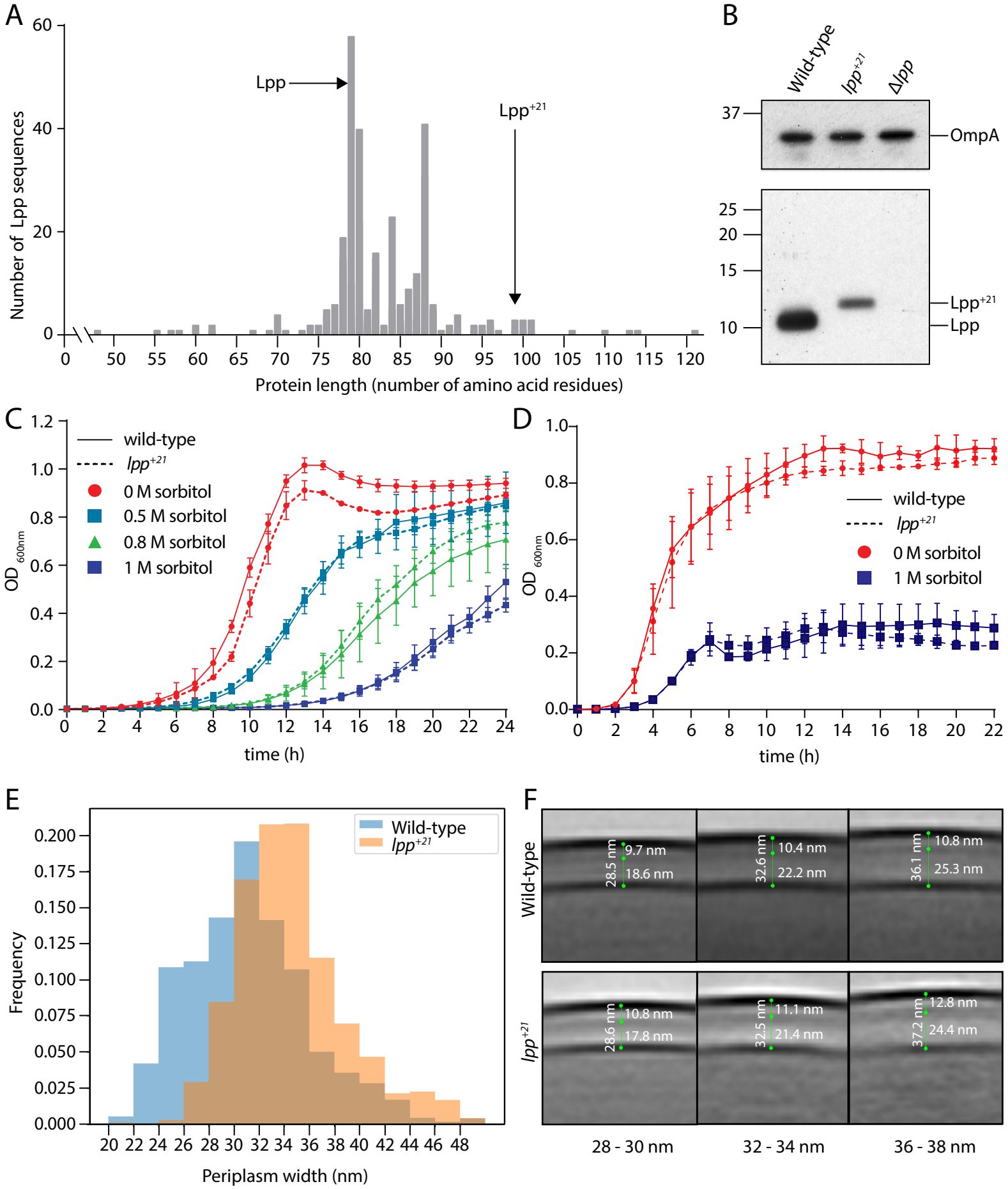

Figure 1. Phenotypes of *E. coli* cells encoding the Lpp+21 isoform. (A) Non-redundant Lpp sequences were identified (Methods) and the protein length charted on the x-axis. The number of non-redundant sequences showing that length is shown on the y-axis. The location of Lpp and the lengthened Lpp+21 are indicated. (B) Whole cell lysates were prepared from the indicated strains and subject to SDS-PAGE and immunoblot analysis with anti-Lpp antibodies and anti-OmpA antibodies. OmpA serves as a loading control. (C) The JW5028 – Keio BW25113 strain with *kan* gene replacing a pseudogene background and isogenic Lpp+21 strain (Fig. S1) were grown over 24 hours. The growth medium is M9, containing the indicated concentration of sorbitol as an osmolyte. (D) Growth rates for the same strains were measured in rich (LB) growth media with and without sorbitol over 20 hours. (E) The periplasmic width distribution of the indicated strains in hyperosmotic conditions. While PG layer in the wild-type strain is a uniform thin electron dense layer, the PG layer in the Lpp+21 strain is more diffuse and thicker. (F) Subtomogram averages of cell envelopes in hyperosmotic conditions. Measurements from EM views evaluate the distance between OM and PG in the Lpp+21 strain micrographs. The histogram depicts the frequency with which a given distance is observed between the OM and PG.

131 ***Cell envelope response to elongated Lpp***

132 To determine the adaptive response to changing the distance constraint between OM and PG, quantitative
133 whole cell proteomics was applied to evaluate the Lpp^{+21} strain. Triplicate samples of the wild-type and Lpp^{+21}
134 strains were processed for analysis by mass spectrometry and we sought to identify those proteins where the
135 steady-state level increases or decreases three-fold or more (Log_2 fold change of ± 1.6) in the Lpp^{+21} strain
136 (Fig. 2A; Table S1). The level of the oligopeptide transporter subunits (OppB, OppC, OppD and OppF) are
137 substantially increased in the Lpp^{+21} strain compared to the wild-type (Table S2). This suggests an increase in
138 PG turnover and an overall increased capacity to recycle PG components, and is consistent with the
139 concomitant increase in AmiC, one of the two major amidases involved in PG remodeling. In addition,
140 proteins implicated in diverse stress-responses (cold shock proteins CspG, CspA, CspI and YdfK, as well as
141 envelope stress protein ZraP and redox stress protein YfcG) were observed at increased steady-state levels in
142 Lpp^{+21} strain (Fig. 2A, Table S2). The greatest decreases were seen in the steady state levels of the GatZABCD
143 proteins involved in galactitol phosphotransferase system and DHAP synthesis (Fig. 2A). The *gatABCD* genes
144 have been shown to be responsive to factors that change *E. coli* cell surface tension [24] and Lpp^{+21} has been
145 reported to significantly decrease cell stiffness [25].

146

147 A decrease was seen in the steady-state level of the Lpp^{+21} isoform in the mutant, to approximately one-eighth
148 the level of Lpp in the wild-type strain (Fig. S2). This is consistent with the relative abundance of Lpp and
149 Lpp^{+21} observed in SDS-PAGE analysis of cell extracts from the two strains (Fig. 1F). However, despite the
150 relative decrease, Lpp^{+21} remains as a highly abundant component of the OM-PG linkage factors given that
151 Lpp is present at up to 10^6 protein molecules per wild-type cell [1, 26].

152

153 The mass spectrometry data was processed to allow for an analysis of sub-cellular proteomes [27] (Fig S3). An
154 initially puzzling observation was that the Lpp^{+21} strain has a 12% overall reduction of total periplasmic
155 protein compared to wild type (Fig. 2B). This was calculated as the proportion of the summed intensity from
156 identified proteins predicted to reside in the periplasm in the STEPdb: G, E, F2, F3, I annotations [27] (Fig S3).
157 Both Lpp^{+21} strains and null Lpp strains of *E. coli* are softer as previously adjudged by atomic force
158 microscopy [25], and factors that increase the softness of *E. coli* also increase outer membrane vesicle (OMV)
159 production [17, 28, 29, 30]. To address whether the measured depletion of periplasmic content reflects an increased
160 production of OMVs, extracts measuring the amount of total protein in the OMV fraction were normalized to
161 OD_{600} (Fig 2C, Fig. S3). This confirmed that the presence of Lpp^{+21} promotes approximately 10-fold more
162 total protein associated with the OMV fraction, reflecting increased OMV production. The overall level of
163 OM proteins associated with the cells was maintained constant (Fig. S3) but a small OM integrity defect was
164 evident from an increased sensitivity to SDS (Fig. 2D).

165

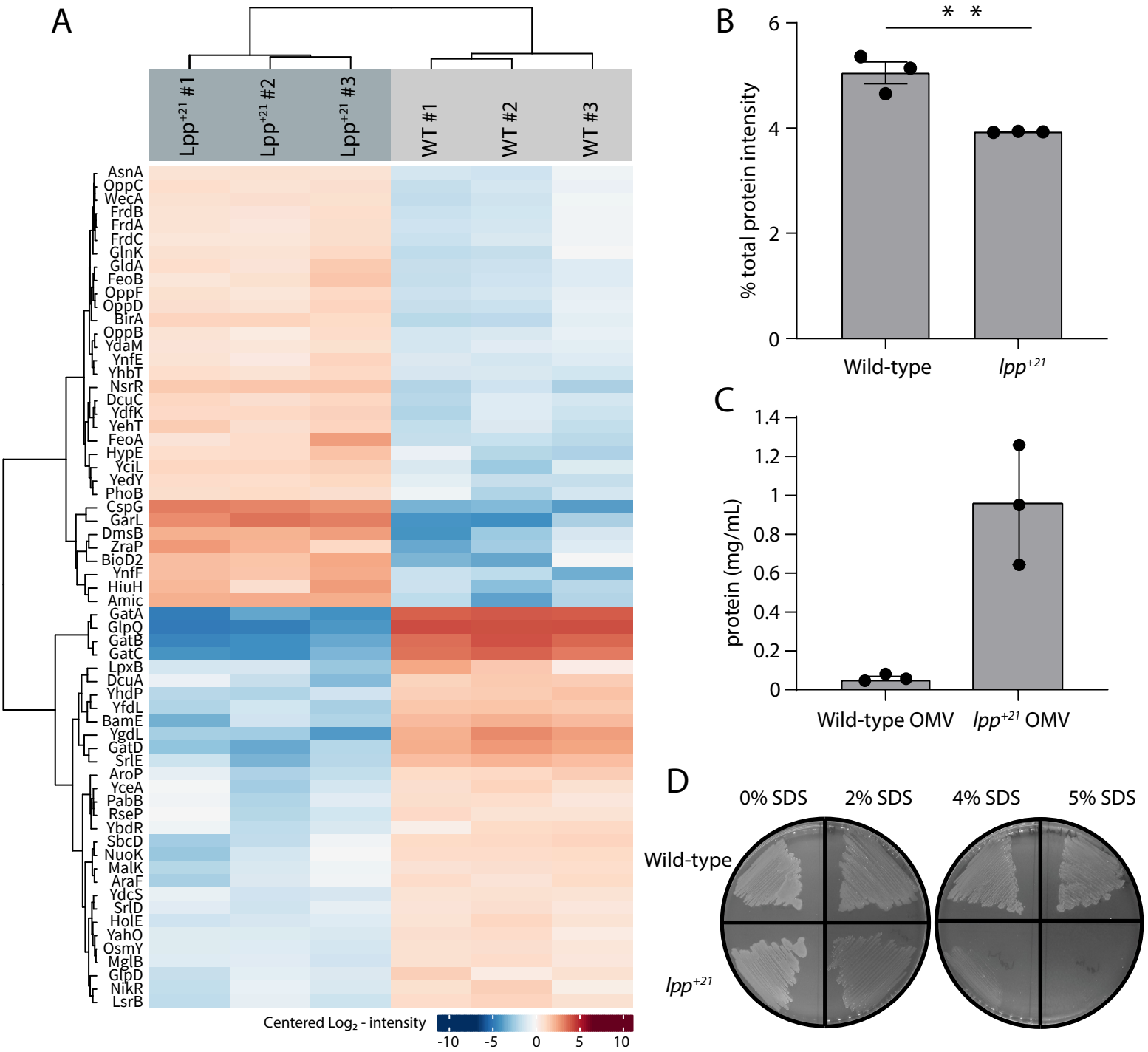

Figure 2. The Lpp+21 cells have softened outer membranes and increased blebbing. (A) Heat map of the significant proteomic differences observed between the wild-type and Lpp+21 mutant. Blue boxes indicate a relative reduction and red indicates a relative increase in protein level, centred on the average of the replicate samples. The grouping of the proteins is based on the similarity of the change in expression observed. (B) The Lpp+21 mutant has an overall reduction in the level of periplasmic proteins. (C) The Lpp+21 mutant has an increase in protein secreted via OMV blebbing. (D) SDS sensitivity profiles of the Lpp+21 mutant compared to the wild-type in increasing concentration of SDS in LB (solid) media. Representative data are shown from experiments performed in triplicate.

167 ***Lpp^{+21} can be accommodated in the periplasm, but other factors become essential***

168 To directly address the altered phenotype induced by Lpp^{+21}, we established a synthetic genetic array for
169 factors in *E. coli* that become essential in order to maintain viability of the Lpp^{+21} strain (Fig S4). The screen
170 demands synthetic growth phenotypes from an array of mutants each lacking a single gene that, while non-
171 essential in wild-type *E. coli*, become essential in the Lpp^{+21} strain of *E. coli*. The endogenous *lpp* gene was
172 replaced by a gene encoding Lpp^{+21} in a isogenic library of 3818 *E. coli* mutants, each of which lacks a non-
173 essential gene. Growth on rich medium allowed the rescue of the new library for array into a format suitable
174 for high-throughput screening with a Singer RoToR robotics platform (Fig S4). Phenotypic analysis was
175 thereafter scored for growth by comparing the growth of the isogenic mutants in the Lpp background (Fig.
176 3A) with the equivalent mutants in the Lpp^{+21} background (Fig. 3B). Each of the genes that displayed a
177 noticeable phenotype in these analyses are presented in Table 1.

178

179 The only cytoplasmic factor identified in our screen, YraN is predicted to be a Holliday-junction resolvase
180 related protein, and we therefore speculate that this mutant failed to resolve the merodiploid condition transient
181 in the introduction of the *lpp*$^{+21}$ condition to the background strain, making the *yraN* mutant a technique-
182 relevant artefact of the screen. This being the case, only functions performed in the periplasm were recovered
183 as essential to viability for the Lpp^{+21} strain.

184

185 Most of the components of the LPS biosynthetic machinery are essential genes in *E. coli* and are thus not
186 represented in the library of non-essential genes. Several non-essential genes in the LPS biosynthetic pathway
187 that are in the library, become essential to the Lpp^{+21} strain (Table 1): the core LPS biosynthesis factors GalU,
188 GmhB and RfaD were shown to be essential in the Lpp^{+21} strain..

189

190 ***An essential role for keeping the OM-PG distance***

191 Several genes encoding proteins that could play roles in anchoring the PG within the cell envelope were
192 identified as essential in the Lpp^{+21} background. Independently, none of the major proteins bridging the OM
193 and PG are essential for growth in *E. coli* [19] and all are therefore represented in the library. In a Lpp^{+21}
194 background the genes encoding the β-barrel protein OmpA and the lipoprotein Pal become essential (Table
195 1). PG-binding domain PF00691 is common to these proteins: appended to a beta-barrel in OmpA, but to a
196 lipoyl anchor in Pal, and is also conserved in other proteins across diverse Gram-negative bacteria (Fig 3C).
197 In *E. coli* there are 4 additional proteins containing this PG-binding domain and these were mapped in a
198 sequence similarity network analysis (Fig 3D). A protein of unknown function, YiaD, is present (Fig 3D) and
199 it too is essential in a Lpp^{+21} background (Table 1). We suggest, therefore, that this protein plays a substantive
200 role in OM-PG linkage. The remaining three proteins: MotB, LafU and YfiB, are more divergent to the
201 OmpA/Pal/YiaD cluster. Neither *motB*, *lafU* nor *yfiB* displayed a synthetic phenotype with Lpp^{+21}, and it has

202 been suggested previously that *motB*, *lafU* and *yfiB* are not expressed at detectable levels under laboratory
203 conditions [31].
204
205 Detecting genes encoding drug-efflux pumps as important for growth of the Lpp^{+21} strain was initially
206 surprising. Either the absence of the inner membrane proteins AcrB or the OM component TolC caused a
207 reduction of growth in the Lpp^{+21} genetic background (Table 1). When antibiotic selection was removed by
208 plating the mutants on medium without chloramphenicol, the synthetic growth defects were observed in the
209 absence of drug selection (Fig. 3D), indicating that this synthetic phenotype is not the result of a decreased
210 drug efflux activity. The trans-envelope AcrAB-TolC multidrug efflux pump has been shown to traverse
211 through the PG and interact directly with PG at several defined sites [32, 33, 34, 35, 36], and as loss of the core AcrB
212 and TolC components became essential, we suggest that this system could be acting as an additional OM-PG
213 linkage that becomes essential in a Lpp^{+21} background. Together with the observation that OmpA, Pal, YiaD
214 and TolC are also essential in the Lpp^{+21} genetic background, these data suggest that functions that maintain
215 local areas of closer contact between the OM and PG are essential for viability.
216

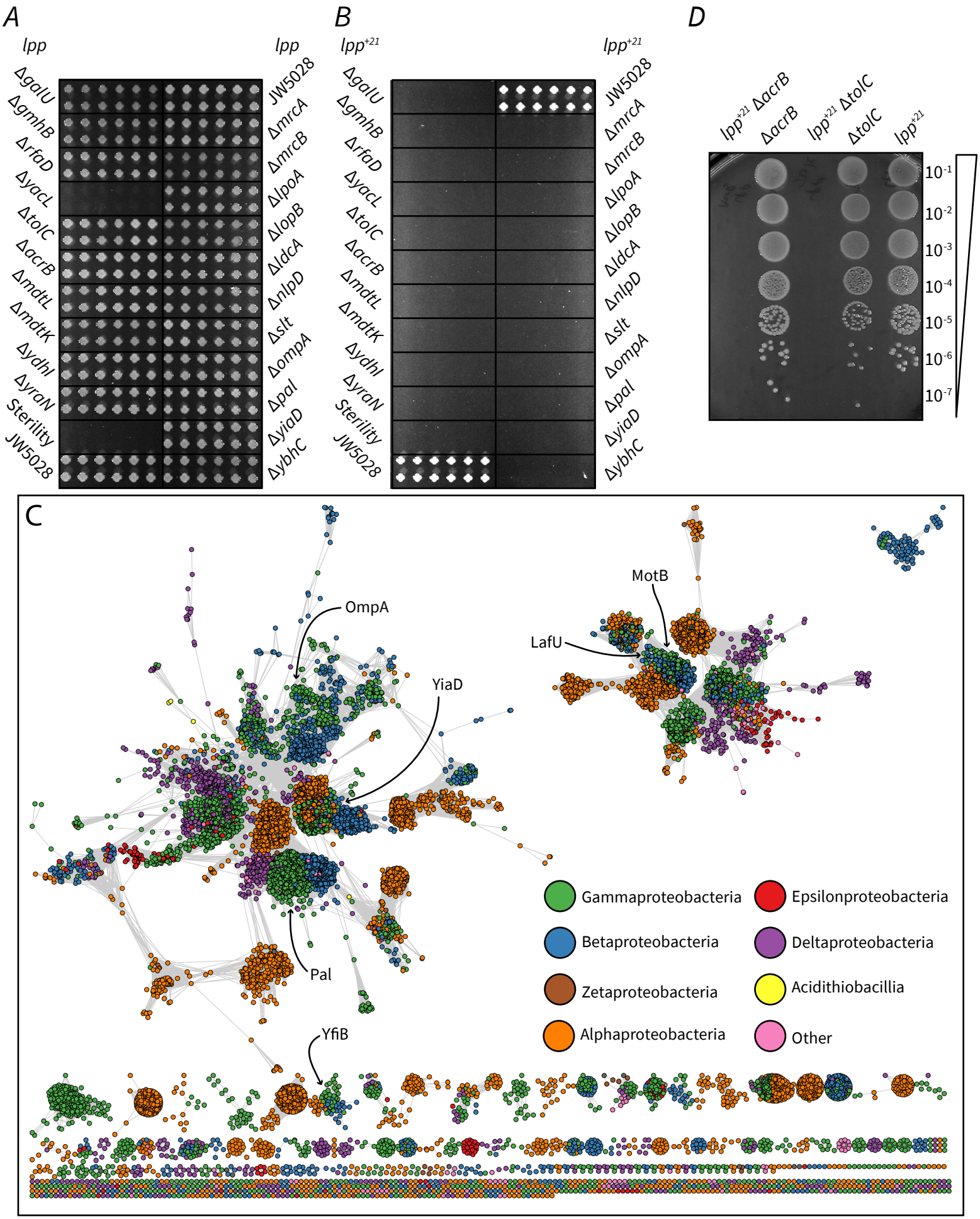

Figure 3. Factors that become essential to mediate OM-PG linkage in Lpp+21 *E. coli.* (A) The growth phenotype in M9 minimal media (0.5 M sorbitol) of single gene knock outs that exhibit essentiality on Lpp+21 background (Table 1). (B) The growth phenotype in M9 minimal media (0.5 M sorbitol) of double gene mutants. The mutants are results of Hfr Cavalli *lpp:lpp*+21 cat crossed with 22 KanR recipients shown in panel A (methods). The double mutants are indicated and are arranged in 4 biological replicates (each having 4 technical replicates). (C) Sequence similarity network of domain (Pfam PF00691) containing proteins from across the Proteobacteria. Each circle represents a protein from a representative proteome (rp35) containing the PF00691 domain, connected by lines with a length imparted by their similarity score as defined by EFI - Enzyme Similarity Tool 68, with a cutoff of 30. Proteins are colored by their taxonomic class and the approximate location of the *E. coli* K12 six PF00691 proteins is indicated. (D) Synthetic lethal phenotype of the drug efflux mutants in the absence of selective antibiotics in M9 minimal media condition. Representative data are shown from experiments performed in biological triplicate.

218 **Table 1. Essential genes in the Lpp^{+21} strain**
219

Cellular process	Lpp^{+21}-essential genes	Function
LPS biosynthesis	*galU*	UDP-glucose metabolic process
	gmhB/yaeD	ADP-L-glycero-β-D-manno-heptose biosynthetic process
	rfaD/hldD/waaD	ADP-L-glycero-β-D-manno-heptose biosynthetic process
Peptidoglycan biosynthesis, turnover and remodelling	*lpoA, lpoB,*	Regulators of PG synthases
	mrcA, mrcB	PG synthases
	ldcA	L,D-carboxypeptidase involved in PG recycling/turnover
	nlpD	Regulator of AmiC PG hydrolase
	slt	Lytic PG transglycosylase, degradation of uncrosslinked glycan strands
	ybhC	Carbohydrate esterase, PG turnover*
PG-OM linkage	*acrB, mdtL*#*, mdtK*#*, ydhI*#	IM components of drug efflux pumps.
	tolC	OM component of drug efflux pump
	ompA	β-barrel protein with PG binding domain
	pal	Lipoprotein with PG binding domain
	yiaD	Lipoprotein with PG binding domain

220 * The function of YbhC is not known, but cellular localization, structural and transcriptomic evidence
221 indicates it may be involved in PG turnover [37]

222 # Putative IM drug efflux machinery, TolC independent with as yet unknown OM component [38]

223

224 To compare the behaviors of Lpp and Lpp^{+21}, both with and without an OmpA monomer present, molecular
225 dynamics (MD) simulations were run for 200 ns each (see Methods for details). The Lpp lipoprotein from *E.*
226 *coli* is a triple coiled-coil that is anchored to the inside face of the outer membrane by its N-terminal acyl
227 group with a length equating to approximately 7.5 nm [39]. The experiments were established to test the scenario
228 for Lpp trimers or Lpp^{+21} trimers in the absence or presence of an OmpA tether between the patch of OM and
229 patch of PG (Fig. 4). These MD simulations only represent a portion of the membrane, and as such we could
230 not account for potential heterogeneity in the protein and LPS concentrations between a WT and Lpp^{+21} cell.
231 For three of the systems: Lpp only, Lpp with OmpA, and Lpp^{+21} only, tilting was marginal, with tilt angles of
232 76.9±4.7°, 75.5±4.7°, and 82.8±2.9°, respectively (all numbers from the last 100 ns of the 200-ns trajectory).
233 These angles are in agreement with previous simulations of Lpp alone (~80°) and Lpp with an OmpA
234 monomer (~75°) PG [36, 40, 41]. In initial simulations of Lpp^{+21} with OmpA, the non-covalent connection between
235 OmpA and PG was quickly disrupted as Lpp^{+21} extended from its kinked state. Therefore, the simulation was
236 repeated with an enforced OmpA-PG connection. Lpp^{+21} was observed to both straighten and tilt within the
237 first 100 ns; the tilt angle measured for the last 100 ns was 49.4±2.3°.
238 .
239 The distance between the OM inner leaflet phosphorus atoms and the PG sugars was measured in each
240 scenario. In the presence of Lpp, the distances with and without OmpA were similar at 8.3±2.1 nm and 8.1±1.2
241 nm, respectively. This was not true for the other scenarios where the distance for Lpp^{+21} alone was 11.6±1.3
242 nm, but for Lpp^{+21} with OmpA, the distance was reduced significantly to 8.7±2.7 nm. Thus, we observe that
243 PG-binding proteins like OmpA can counteract the increased distance imposed by Lpp^{+21}, inducing it to tilt
244 significantly in accommodation. We also compared our simulations to the distances that were measured by
245 EM (centre of the OM to centre of the PG). In wild-type *E. coli* (i.e. Lpp+OmpA), the centre-centre distance
246 in the simulations is 10.7 +/- 2.2 nm (Fig 4B), similar to the 9.7 -10.8 nm measured in intact cells (Fig. 1F).
247 The centre-centre distance measured in the simulation of Lpp^{+21} tilted by the presence of OmpA (11.0 +/- 2.6
248 nm), fits the observed distances of 10.8 – 12.8 nm much better than the distance that would be created by a
249 perpendicular Lpp^{+21} (14.2 +/- 1.3 nm).

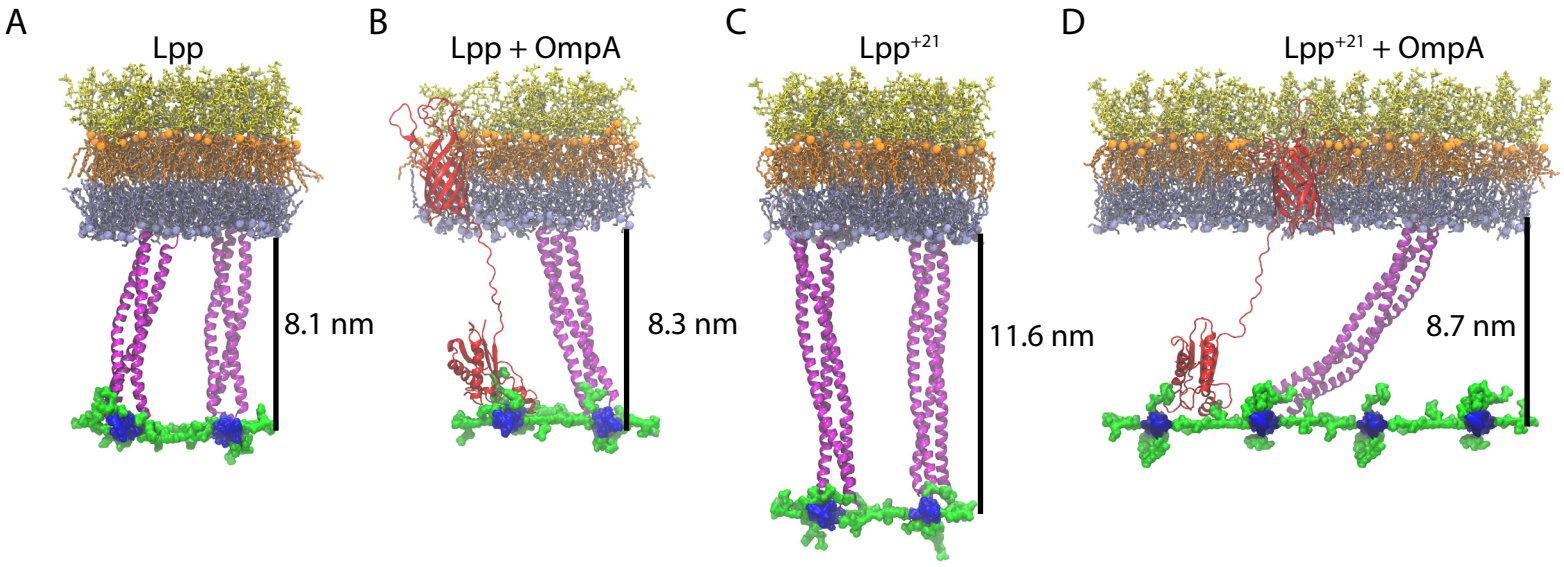

Figure 4. Final states of the OM-PG linkage from MD simulations. (A-B). A patch of OM with the LPS molecules depicted in orange (lipid A moiety) and yellow (core oligosaccharides), and the phospholipids in the inner leaflet of the OM depicted in grey. The PG layer (blue for glycans and green for peptide crosslinks) is attached to the OM via two trimers of Lpp (A), or a trimer of Lpp and the PG-binding domain of OmpA (red). The β-barrel anchor of OmpA is shown embedded in the OM. (C-D) Equivalent scenarios formed with Lpp+21 trimers. The distances shown are calculated from the inner face of the OM to the centre of the PG layer and represent the average over the last 100 ns of a 200-ns simulation

251 **DISCUSSION**

252

253 We observed that over a range of osmotic conditions, and in nutrient-rich or nutrient-poor media, growth rates
254 of the Lpp^{+21} strain of *E. coli* were equivalent to the isogenic wild-type *E. coli*, suggesting bacteria can adapt
255 to the presence of the extended Lpp^{+21}. We observed a moderate increase to the OM-IM space similar to that
256 previously reported [17, 18, 25] and reviewed [25, 42]. Three adaptive features were expressed as phenotypes in the
257 Lpp^{+21} strain: (i) the steady-state level of the Lpp^{+21} tether was reduced eight-fold compared to the level of
258 Lpp in the isogenic wild-type strain, and other tethers that enforce a wild-type distance: OmpA, Pal, YiaD and
259 TolC, became essential factors in the Lpp^{+21} condition, (ii) structures that depend on a wild-type OM-IM
260 distance, such as the LPS transport system, continued to function but key components of the system became
261 essential for cell viability, and (iii) the PG network took on characteristics of dysregulated synthesis and all
262 components of an otherwise redundant PG biosynthesis pathway become essential to viability. In response to
263 Lpp elongation we demonstrated a reduction in Lpp levels, as shown by the quantitative proteomic presented
264 here, and the apparent tilting of the elongated Lpp as suggested by our molecular dynamic simulation. The
265 reduction in the copy number of the elongated Lpp isoform observed in the quantitative proteomics was not
266 due to differences in transcriptional regulation, as RNAseq data demonstrated a moderate increase in the level
267 of lpp^{+21} transcripts in the mutant (Table S6). Taken together, this may suggest a reinterpretation of some of
268 the previous conclusions drawn from experiments with elongated Lpp isoforms that assumed that Lpp^{+21} was
269 present at the same amount as Lpp, and that Lpp^{+21} sits perpendicular to the membranes and thereby the 21
270 extra amino acids always stretch the periplasmic width by a constant amount [17, 18, 25].

271

272 ***Tethers that enforce the distance constraint between the OM and PG layer became essential factors in the***
273 ***Lpp^{+21} condition***

274 The lipoyl-N-terminus of Lpp is integrated into the OM, and the C-terminus of a protomer of the Lpp trimer
275 is covalently linked to the PG layer. Stereochemically, only one unit of a Lpp trimer can be covalently attached
276 to the PG layer, and this stoichiometry has been observed experimentally [39, 40, 43]. This makes each Lpp trimer
277 an important bridge between the OM and PG layers of the cell wall, but it has not been clear whether the core
278 role of Lpp is acting in compression or tension. In other words [44], is the role of Lpp to be a supportive brace
279 to keep the OM away from the PG, or a binding anchor to bring the OM as closely as possible to the PG? In
280 a wild-type *E. coli* scenario, molecular dynamics simulations show that the flexible linkers in PG-binding
281 proteins like OmpA allow for adjustments in positioning the PG relative to the OM. In the presence of Lpp,
282 the flexible linker of the PG binding domain of OmpA needs to extend further from the OM, as the distance
283 between the OM and PG increases when Lpp sits perpendicular to the OM [40]. In the absence of Lpp, OmpA
284 determines the distance between the OM and PG [40, 41], but is not essential for cell viability [45, 46]. Taken together
285 with the data presented here from characterization of the Lpp^{+21} phenotypes, we suggest that Lpp functions as
286 a brace to keep the OM away from the PG layer.

287

288 The genetic screen showed that each one of the OM-located PG-binding factors Pal, YiaD and OmpA are
289 essential (as is TolC) for viability of the Lpp^{+21} strain of *E. coli*. While previous high throughput synthetic
290 genetic screens, demonstrate none of Pal, YiaD, OmpA nor TolC are essential or negatively affect the growth
291 in an Lpp null background [45, 46]. The overlap in the distance constraints measured for cells expressing Lpp and
292 Lpp^{+21} suggests that much of the Lpp^{+21} is in the highly tilted (49.4±2.3°) form observed in the MD
293 simulations. The enforced tilt and reduction in steady state levels of Lpp^{+21} would severely impact its bracing
294 force, with the measurable consequence that membrane integrity (SDS resistance) is diminished, OmpA and
295 other tethers become essential to viability, and the OM is highly permissive to OMV formation. Furthermore,
296 the discovery of YiaD in the genetic screen for essential factors is significant. Our proteomic assessment and
297 previously published data [26] demonstrated that the copy number of YiaD is much lower than that of either Pal
298 or OmpA, making it not immediately clear how a minor component of the membrane could be exerting such
299 an essential role. Previously, YiaD was suggested to be a factor regulating OMP biosynthesis by the BAM
300 complex [47]. Structural analysis shows YiaD to be highly similar to the PG-binding domains of Pal and OmpA
301 [48]. We suggest that the primary function of YiaD is to mediate OM-PG linkage, and that this indirectly impacts
302 on OMP biogenesis.

303

304 ***Continued function of LPS transport in localized regions of the periplasm***

305 The bridges needed to mediate LPS transport appear to be susceptible to disruption caused by Lpp^{+21} in *E.*
306 *coli*. LptA is subject to degradation if the Lpt complex is compromised [7], with LptA-LptC and LptA-LptD
307 interactions proposed as key quality control steps in the assembly of the Lpt complex [6]. That the Lpp^{+21} cells
308 have enough maintained sufficient LPS in the OM to maintain membrane integrity is supported by our
309 observations of the only minor increase in SDS sensitivity of the strain and observations by others of only
310 minor changes in vancomycin sensitivity [25]. These findings are consistent with observations through electron
311 microscopy that regions of the periplasm in Lpp^{+21} cells are maintained with OM-PG distances reflective of
312 the wild-type condition, which would permit LPS transport to the OM.

313

314 ***All components of the PG biosynthesis pathways become essential to cell viability***

315 In *E. coli*, the weave of the PG-layer is maintained in a uniform, open state through quality control mechanisms
316 that depend on the regulators in the OM (LpoA and LpoB) being able to permeate it to contact the synthetases
317 (PBP1a and PBP1b) in the IM. It has been hypothesized in this way that the OM lipoproteins may serve as a
318 molecular ruler to modulate PG thickness, maintaining a single layer of PG equidistant from the OM layer
319 under normal conditions [11]. The PG synthases encoded by *mrcA* and *mrcB* are redundant in the sense that
320 *mrcA* mutant strains and *mrcB* mutant strains are each viable [49, 50, 51]. However, in the Lpp^{+21} strain both *mrcA*
321 and *mrcB* (as well as their OM lipoprotein partners) are essential for viability, indicative of a compromised
322 capability to build the PG-layer. Mutations designed to impact on these interactions lead to transient deposition

323 of "high-density PG" and "multi-layered PG" through dysregulation of the synthetases [11]. The broader and
324 more diffuse morphology of the PG-layer observed by electron microscopy in the Lpp^{+21} strain could suggest
325 a similar phenotype associated with transient or local impacts on the OM-PG distance [11]. It's worth noting
326 Δ*lpp* Δ*mrcB* mutants have previously shown a moderate growth defect [52] and that this defect could be
327 alleviated with the introduction of the *lpp*$^{+21}$ gene [18], whereas in the present study we observed a synthetic
328 lethal phenotype in the Δ*mrcB lpp*$^{+21}$ mutants. This discrepancy could be due differences in growth conditions
329 used (LB vs hyperosmotic minimal media) imparting additional periplasmic stress or differences in the strain
330 background (DH300 vs BW25113).
331
332 An essential requirement was also placed on PG-layer remodeling, whereby the PG-binding factor NlpD was
333 found to be essential in Lpp^{+21} cells: its function is in modulating the activity of the amidase AmiC [53, 54] to
334 remodel PG strands, and AmiC was observed at increased steady-state levels in the Lpp^{+21} strain. Taken
335 together with the increase in oligopeptide transporter subunits (OppB, OppC, OppD and OppF) in the Lpp^{+21}
336 strain to recycle PG precursors across the IM, our results suggest a clearance of the malformed PG caused by
337 dysregulation of the PG synthases is a crucial adaptation in the Lpp^{+21} strain.
338
339 ***Stiffness, load-bearing and connection of OM-PG***
340 The concept of bacterial cell stiffness has emerged as a means to understand the physical parameters that
341 define how readily bacteria can respond to major environmental changes [30, 55, 56]. Measurements by AFM have
342 revealed a characteristic stiffness in Gram-negative bacterial cells that is contributed by load-bearing outer
343 membrane and its attachment to the underlying PG layer [57]. In *E. coli*, mutants lacking Lpp, Pal or OmpA are
344 softer than wild-type cells [57], and cells expressing the Lpp^{+21} isoform are also softer than wild-type cells [25].
345 Taken together with our observation that the Lpp^{+21} isoform display a broader and more diffuse PG layer
346 morphology in the subtomogram averages, this further supports the proposition that the OM is a major
347 contributor to cell stiffness [55, 57].
348
349 Although Lpp length alone does not appear to dictate periplasm width, indeed the *Pseudomonas aeruginosa*
350 Lpp protein is only 4 amino acids longer than that of *E. coli* but its periplasm has been measured as ~3 nm
351 larger under identical conditions [58], the length of Lpp seen in *E. coli* is conserved in a range of bacterial
352 lineages. The species from the genus *Geobacter* naturally express longer Lpp proteins of 99 or more residues,
353 equivalent to Lpp^{+21} in length. *Geobacter* species have a complicated periplasm housing "electron conduits"
354 formed of transmembrane and periplasmic redox proteins, in order to transfer electrons to the external surface
355 of the bacterial cell [59, 60]. There have been no direct measurements of the width the periplasm of *Geobacter*,
356 but it would be interesting to see if these naturally longer Lpp forms correlates with an enlarged periplasm.
357 That species of *Geobacter* serve as an exception to what is otherwise a strict rule about the length of Lpp, and
358 thus the structurally-enforced distance constraint between the OM and PG layer, raises interesting questions

359 about whether OM softness, OMV production or increased OM permeability might assist the unusual
360 biological functions of the OM and periplasm in bacteria other than *E. coli*.
361

362 **MATERIALS AND METHODS**

363

364 ***Bacterial strains and growth conditions***

365 *E. coli* BW25113 was the parental strain of all the recipient strains used in this study. JW5028, a derivative of
366 BW25113, containing a kanamycin resistance marker in place of a pseudogene, was used as the wild-type for
367 this study. Strains were grown in LB broth or M9 minimal media broth supplemented with 1 mM $MgSO_4$,
368 0.1mM $CaCl_2$, 1.12 mM thiamine and 0.2% (w/v) glucose for a defined minimal media. To osmotically
369 stabilize the growth medium, sorbitol was supplemented to a final concentration of 0.5 M. For overnight
370 cultures, strains were grown in LB broth overnight at 37 °C under continuous agitation. Subculturing was
371 done by diluting the saturated culture 1:100 using new media. The cells were then grown to mid-exponential
372 growth phase (OD_{600} = 0.5-0.6) at 37 °C under shaking. Culture media was supplemented with antibiotics for
373 plasmid selection and maintenance or selection of mutants at the following concentrations: 100 µg/ml
374 ampicillin, 30 µg/ml kanamycin, 34 µg/ml chloramphenicol. 15 g/l agar was added to media before
375 autoclaving when solid media was required (Fig. S4).

376

377 ***Construction of Lpp^{+21} mutant***

378 The endogenous *lpp* gene was replaced with the extended *lpp*$^{+21}$ gene previously described [17, 18] with minor
379 modifications (Fig. S1). First the replacement was done in the donor *E. coli* Hfr Cavalli cells using the λ –red
380 recombination system [61]. A gene block was sourced (Integrated DNA Technologies) containing extra 21 amino
381 acid residues (three heptad repeats) inserted between codon 42 and 43 of *E. coli* Lpp. The gene block also
382 contained 50 bp DNA flanking 5' and 3' ends of the *lpp*$^{+21}$ gene. On the 5' end, the extension was homologous
383 to DNA sequence upstream of *lpp*, while on the 3' end, the extension was homologous to the *cat* gene. The
384 gene block was combined with the *cat* gene by Gibson assembly, and the resulting PCR fragment was used to
385 replace *lpp.* The new Lpp^{+21} strain was selected by plating on medium containing chloramphenicol.
386 Chromosomal *lpp*$^{+21}$ was moved into *E. coli* BW25113 background by mating with kanamycin-resistant Keio
387 collection strain JW5028, described above, to generate a double mutant [19, 62] (Fig. S4). The mutation was
388 verified by PCR described (Fig. S1) and sequencing.

389

390 ***SDS-PAGE and immunoblotting***

391 Cells grown in M9 minimal media (0.5 M sorbitol) and normalized by OD_{600nm}, lysed in Laemmli SDS-loading
392 dye and separated in 15% acrylamide gels and transferred to 0.45 µm hydrophobic Immobilon-P PVDF
393 membrane (Merck Millipore). Immunoblotting was as described previously [19]. Rabbit primary antibodies; α-
394 Lpp antibody (kindly provided by T. Silhavy) and α-OmpA were diluted 1:400,000 and 1: 30,000, respectively
395 in 5% skim milk, TBST. The membranes were incubated with goat, α-rabbit IgG, HRP-conjugated secondary
396 antibody (Sigma; 1: 20,000 in 5% skim milk, TBST), and washed with TBST. Detection was by enhanced

397 chemiluminescence with ECL prime western blotting detection reagent (GE Healthcare Life Sciences),
398 visualized using Super RX-N film (Fujifilm).
399
400 ***Outer membrane vesicle purification and quantification***
401 Overnight cultured cells, grown in LB without antibiotics, were washed twice in 1 x M9 salts then subcultured
402 in 500 ml M9 minimal media supplemented with 0.5 M sorbitol (1:1000 dilution). The strains were grown to
403 late logarithmic phase without antibiotics, $OD_{600} \approx 0.9$ and spun down to collect culture supernatant. Collected
404 culture supernatant were then processed for OMVs isolation and purification using differential
405 ultracentrifugation technique as discussed previously [63]. OMVs were washed twice in PBS to remove sorbitol
406 then quantified using a bicinchoninic acid assay kit (Thermo Scientific CST#23225).
407
408 ***SDS sensitivity***
409 Streaks were made on LB (solid) media with 0% SDS – 5% SDS. After 16 hrs of incubation at 37 °C, the
410 minimum SDS concentration inhibiting growth was obtained by analyzing growth on each concentration. The
411 streaks were done in duplicate and repeated three times.
412
413 ***Proteomics***
414 Saturated overnight cultures were washed twice in 1 x M9 salts and diluted 1:100 in 10 ml M9 minimal media
415 supplemented with 0.5 M sorbitol. Cultures were further grown to logarithmic phase, collected by
416 centrifugation and washed using PBS buffer. The cell pellet was homogenised in 4 % SDS, 100 mM Tris, pH
417 8.1 and boiled at 95 °C for 10 minutes. The lysate was then sonicated with a Bioruptor® Pico (Diagenode)
418 and protein concentration was determined with Bicinchoninic Acid assay (BCA, Thermo Fisher). SDS was
419 removed with chloroform/methanol, the protein was digested by trypsin overnight and the digested peptides
420 were purified with ZipTips (Agilent). Using a Dionex UltiMate 3000 RSLCnano system equipped with a
421 Dionex UltiMate 3000 RS autosampler, an Acclaim PepMap RSLC analytical column (75 µm x 50 cm,
422 nanoViper, C18, 2 µm, 100Å; Thermo Scientific) and an Acclaim PepMap 100 trap column (100 µm x 2 cm,
423 nanoViper, C18, 5 µm, 100Å; Thermo Scientific), the tryptic peptides were separated by increasing
424 concentrations of 80% ACN / 0.1% formic acid at a flow of 250 nl/min for 120 min and analyzed with a
425 QExactive Plus mass spectrometer (Thermo Scientific). The instrument was operated in the data dependent
426 acquisition mode to automatically switch between full scan MS and MS/MS acquisition. Each survey full scan
427 (m/z 375–1575) was acquired in the Orbitrap with 60,000 resolution (at m/z 200) after accumulation of ions
428 to a 3×10^6 target value with maximum injection time of 54 ms. Dynamic exclusion was set to 30 seconds.
429 The 20 most intense multiply charged ions ($z \geq 2$) were sequentially isolated and fragmented in the collision
430 cell by higher-energy collisional dissociation (HCD) with a fixed injection time of 54 ms, 15,000 resolution
431 and automatic gain control (AGC) target of 2×10^5.
432

433 The raw data files were analyzed using MaxQuant software suite v1.6.5.0 [64] against Andromeda search engine
434 [65] for protein identification and to obtain their respective label-free quantification (LFQ) values using in-house
435 standard parameters. The proteomics data was analyzed using LFQ-Analyst [66] and the analysis of the data
436 quality analysis is presented in Fig S6. Due to the 21 amino acid insertion in the Lpp^{+21} isoform, the relative
437 levels of Lpp in the mutant had to be assessed manually. Only the unique peptide (IDQLSSDVQTLNAK)
438 shared between the two isoforms was used to quantify the levels of Lpp and Lpp^{+21} in the wild-type and mutant
439 strain, respectively (Fig S2).
440
441 To estimate the total relative amount of proteins from the various subcellular compartments, the raw intensities
442 from peptides identified from proteins from different subcellular locations were summed and divided by the
443 total summed intensity from all peptides. Sub-cellular locations annotations were applied from the STEPdb
444 2.0 [27] where proteins designated F1, A, R, and N were classified as cytoplasmic; B was designated inner
445 membrane; H, X, and F4 were designated outer membrane / extracellular; and I, G F2, F3, and E were
446 designated as periplasmic.
447
448 ***Sequence similarity network analysis***
449 Proteobacterial proteins containing the Pfam domain (PF00691) were extracted from the Representative
450 Proteome 35% co-membership rpg-35 group [67] and a sequence similarity network was generated with the EFI
451 Enzyme Similarity Tool [68]. This network was visualized with Cytoscape [69] with a similarity score cutoff of
452 30. Each protein is represented by a colored circle node and each similarity match above the similarity score
453 cutoff is represented by an edge between nodes with the length determined by the similarity score.
454
455 ***Lpp length distribution across bacterial species***
456 To determine the amino acid length distribution of Lpp in Gammaproteobacteria (Table S4), amino acid
457 sequences were sourced from the InterPRO database (version 81.0) [70] using the Interpro Family tag - Murein-
458 lipoprotein (IPR016367). Filtered Lpp sequences were then concatenated into representative nodes (at least
459 >90% sequence similarity) using the online available amino acid Initiative-Enzyme Similarity Tool (EFI-EST)
460 [68].
461
462 ***Synthetic genetic interaction array***
463 The Lpp^{+21} isoform was transferred to each of the Keio collection clones by conjugation as described (Fig.
464 S4). First, the Hfr chloramphenicol resistant Lpp^{+21} strain was arrayed in 384-colony density on LB agar
465 containing chloramphenicol using the Singer rotor HAD (Singer Instruments, United Kingdom). Similarly,
466 the Keio collection arrayed in 384-colony density was pinned on LB agar plates containing kanamycin and
467 incubated overnight at 37 °C. Using the Singer rotor HDA, the Hfr Lpp^{+21} strain and the Keio collection clones
468 from the 384-colony density were then co-pinned onto LB agar plates and incubated at 37 °C for 16 hours.

469 Following conjugation, the colonies were transferred to LB agar with kanamycin (selection 1) at the same
470 colony density and incubated at 37 °C for 16 hours. To select for double mutants (selection 2), colonies from
471 the intermediate selection were pinned on LB agar with both kanamycin and chloramphenicol and incubated
472 at 37 °C for 14 hours. For assessment of synthetic genetic interaction in nutrient-limited media, the double
473 mutants generated were replica pinned in M9 minimal media at the same density and incubated at 37 °C for
474 25-30 hours. Images were acquired using Phenobooth (Singer Instruments, United Kingdom) for analysis.
475 Images were manually screened to cross-reference recipient plate images to the final double antibiotic
476 selection plates images. Candidate synthetic lethal or growth-compromised mutants were then subjected to
477 another round of screening in the same conditions as previously identified (mini-screen) for validation. Four
478 biological replicates were included that were further arrayed in four technical replicates. Mutants were
479 confirmed by PCR. Where further phenotypic screening of mutants was conducted, independent isogenic
480 knock-out mutants were generated using the PCR and λ-red based homologous recombination method [61].
481
482 Since the Keio collection *yiaD* mutant has been identified as containing a potential duplication event [71], the
483 candidate *yiaD* synthetic lethal interaction was confirmed through independently constructing a *yiaD* mutant
484 in the BW25113 strain background (Fig. S5). The lpp^{+21} variant was subsequently generated in this mutant as
485 described above. As with the Keio *yiaD* mutant, this strain demonstrated synthetic lethality on M9 media.
486
487 Two colony PCR reactions [61, 71] (Fig. S4) confirmed the identity of all candidate double mutants, using a set
488 of primers flanking the *lpp* gene, and a set of primers flanking the kanamycin gene (Table S5).
489
490 ***Preparation of Electron Cryo-microscopy samples, data collection and analysis***
491 Strains were grown aerobically in M9 minimal media (0.5 M sorbitol) until an OD_{600} of 0.6 was reached. Cells
492 were collected by spinning at 6000xg for 5 minutes and resuspended to an OD_{600} of ≈ 12. Cryo-EM, data
493 collection and analysis were performed similarly to previous studies [17, 18], except using 3-D subtomogram
494 averages derived from whole-cell cryotomograms instead of projection images so as to discern peptidoglycan.
495 Tilt series of WT and Lpp^{+21} strains was acquired on an FEI Krios operating at 300 keV with a Gatan K2
496 direct detector and energy filter with a 20eV slit with a tilt range of +/- 60° using 3° increments and
497 reconstructed using IMOD. Subtomograms were picked manually using 3DMOD along the length of all non-
498 polar periplasm and averaged using PEET.
499
500 ***Generation of simulation systems***
501 Initially, two systems were generated: the OM and PG, as previously detailed [56], with two copies of wild-type
502 Lpp and with two copies of Lpp^{+21}. For wild-type Lpp, we used the homo trimer from PDB 1EQ7 [39]. For
503 Lpp^{+21}, a monomer was first built using I-TASSER [72]. Next, the trimer of Lpp^{+21} was built using the wild-type
504 Lpp trimer as a template, further optimized using Targeted Molecular Dynamics (TMD) for 1 ns. For both

505 Lpp and Lpp^{+21}, the proteins were anchored in the OM via N-terminal acylation while the C-terminus of one
506 copy from each trimer was covalently linked to the PG. The systems generated were prepared for equilibration
507 using the following steps for 1 ns each: 1) minimization for 10,000 steps, 2) melting of lipid tails, 3) restraining
508 only the PG and the protein, and 4) restraining the PG and the protein backbone. Both systems were
509 equilibrated for 200 ns.
510 For each of the two systems (Lpp and Lpp^{+21}), a new system was constructed with one Lpp trimer removed
511 and OmpA inserted into the OM. The full-length OmpA structure was taken from Ortiz-Suarez *et al.* [73]. The
512 periplasmic domain region of the OmpA (clamp, hereafter) was lowered to the PG by shortening the distance
513 between the PG and the clamp for 20 ns. After the clamp was lowered, it was clenched to the nearest DAP
514 residue by using two different distance collective variables [74] between the centre of mass of residue 242 or
515 256 from OmpA and that of a nearby PG DAP residue to maintain the connection for 110 ns. In the case of
516 Lpp^{+21}, PG was first pulled towards the OM to match the distance between them in wild-type Lpp, after which
517 the clamp of OmpA was lowered and clenched for 110 ns. The wild-type Lpp/OmpA system was equilibrated
518 for 200 ns; OmpA stayed bound to the PG without colvars. The Lpp^{+21}/OmpA system was also equilibrated
519 for 200 ns, but colvars were needed to maintain the OmpA-PG interaction.
520
521 ***Molecular Dynamics (MD)***
522 All-atom molecular dynamics simulations were performed using NAMD 2.11 [75] and the CHARMM36m [76]
523 and CHARMM36 [77] force-field parameters for proteins and lipids, respectively, with the TIP3P-CHARMM
524 water model [78]. Unless otherwise stated, all MD simulations were performed under a periodic boundary
525 condition with a cut-off at 12 Å for short-range electrostatic and Lennard-Jones interactions with a force-based
526 switching function starting at 10 Å. For long range electrostatic calculations, the particle-mesh Ewald method
527 [79] with a grid spacing of at most 1 Å was used for long-range electrostatic calculations. Bonds between a heavy
528 atom and a hydrogen atom were maintained to be rigid, while all other bonds remain flexible. Unless otherwise
529 stated, each system was equilibrated under an isothermal-isobaric ensemble (NPT) at 310 K and 1 bar, with a
530 timestep of 4 fs after hydrogen mass repartitioning [80]. A Langevin thermostat with a damping coefficient of 1
531 ps^{-1} was used for temperature control and a Langevin piston was used for pressure control. VMD was used for
532 all visualization and analysis [81].
533

ACKNOWLEDGEMENTS

We are grateful to Rebecca Bamert and Jonathan Wilksch for critical comments on the manuscript. The authors thank Andrea Nans and Peter Rosenthal at the Francis Crick Institute for electron microscopy services, and support staff at the Monash Proteomic & Metabolomic Facility. We acknowledge research support from the Australian Research Council (FL130100038 to T.L. and I.D.H.). E.M. was recipient of a Monash Research Scholarship. J.C.G. acknowledges support from the US National Institutes of Health (R01-GM123169). Computational resources were provided through XSEDE (TG-MCB130173), which is supported by the US National Science Foundation (NSF; ACI-1548562). This work also used the Hive cluster, which is supported by the NSF (1828187) and is managed by PACE at the Georgia Institute of Technology.

544 **FIGURE LEGENDS**

545

546 **Figure 1**. **Phenotypes of *E. coli* cells encoding the Lpp^{+21} isoform.** (A) Non-redundant Lpp sequences were
547 identified (Methods) and the protein length charted on the x-axis. The number of non-redundant sequences
548 showing that length is shown on the y-axis. The location of Lpp and the lengthened Lpp^{+21} are indicated. (B)
549 Whole cell lysates were prepared from the indicated strains and subject to SDS-PAGE and immunoblot
550 analysis with anti-Lpp antibodies and anti-OmpA antibodies. OmpA serves as a loading control. (C) The
551 JW5028 – Keio BW25113 strain with *kan* gene replacing a pseudogene background and isogenic Lpp^{+21} strain
552 (Fig. S1) were grown over 24 hours. The growth medium is M9, containing the indicated concentration of
553 sorbitol as an osmolyte. (D) Growth rates for the same strains were measured in rich (LB) growth media with
554 and without sorbitol over 20 hours. (E) The periplasmic width distribution of the indicated strains in
555 hyperosmotic conditions. While PG layer in the wild-type strain is a uniform thin electron dense layer, the PG
556 layer in the Lpp^{+21} strain is more diffuse and thicker. (F) Subtomogram averages of cell envelopes in
557 hyperosmotic conditions. Measurements from EM views evaluate the distance between OM and PG in the
558 Lpp^{+21} strain micrographs. The histogram depicts the frequency with which a given distance is observed
559 between the OM and PG.

560

561 **Figure 2**. **The Lpp^{+21} cells have softened outer membranes and increased blebbing.** (A) Heat map of the
562 significant proteomic differences observed between the wild-type and Lpp^{+21} mutant. Blue boxes indicate a
563 relative reduction and red indicates a relative increase in protein level, centred on the average of the replicate
564 samples. The grouping of the proteins is based on the similarity of the change in expression observed. (B) The
565 Lpp^{+21} mutant has an overall reduction in the level of periplasmic proteins. (C) The Lpp^{+21} mutant has an
566 increase in protein secreted via OMV blebbing. (D) SDS sensitivity profiles of the Lpp^{+21} mutant compared
567 to the wild-type in increasing concentration of SDS in LB (solid) media. Representative data are shown from
568 experiments performed in triplicate.

569

570 **Figure 3. Factors that become essential to mediate OM-PG linkage in Lpp^{+21} *E. coli*.** (A) The growth
571 phenotype in M9 minimal media (0.5 M sorbitol) of single gene knock outs that exhibit essentiality on Lpp^{+21}
572 background (Table 1). (B) The growth phenotype in M9 minimal media (0.5 M sorbitol) of double gene
573 mutants. The mutants are results of Hfr Cavalli *lpp:lpp^{+21} cat* crossed with 22 Kan^{R} recipients shown in panel
574 A (methods). The double mutants are indicated and are arranged in 4 biological replicates (each having 4
575 technical replicates). (C) Sequence similarity network of domain (Pfam PF00691) containing proteins from
576 across the Proteobacteria. Each circle represents a protein from a representative proteome (rp35) containing
577 the PF00691 domain, connected by lines with a length imparted by their similarity score as defined by EFI -
578 Enzyme Similarity Tool [68], with a cutoff of 30. Proteins are colored by their taxonomic class and the
579 approximate location of the *E. coli* K12 six PF00691 proteins is indicated. (D) Synthetic lethal phenotype of

580 the drug efflux mutants in the absence of selective antibiotics in M9 minimal media condition. Representative
581 data are shown from experiments performed in biological triplicate.
582
583 **Figure 4. Final states of the OM-PG linkage from MD simulations.** (A-B). A patch of OM with the LPS
584 molecules depicted in orange (lipid A moiety) and yellow (core oligosaccharides), and the phospholipids in
585 the inner leaflet of the OM depicted in grey. The PG layer (blue for glycans and green for peptide crosslinks)
586 is attached to the OM via two trimers of Lpp (A), or a trimer of Lpp and the PG-binding domain of OmpA
587 (red). The β-barrel anchor of OmpA is shown embedded in the OM. (C-D) Equivalent scenarios formed with
588 Lpp^{+21} trimers. The distances shown are calculated from the inner face of the OM to the centre of the PG layer
589 and represent the average over the last 100 ns of a 200-ns simulation.
590

591 **SUPPLEMENT**

592

593 **Figure S1**. **Construction and assessment of Lpp^{+21} *E. coli*.** (A) Schematic representation of the elongated
594 Lpp^{+21} isoform. The strain was constructed by inserting (red lettering) heptad repeats between residue D42
595 and Q43 of Lpp. (B) Schematic detailing the isogenic replacement of the *lpp* gene with the *lpp*$^{+21}$ gene. (C)
596 PCR confirmation of the *lpp*$^{+21}$ mutant strain (Methods).

597

598 **Figure S2. Quantitation of Lpp and Lpp^{+21} isoforms.** The sequence of the 21 residues inserted to create the
599 Lpp^{+21} isoform is also indicated. Mass spectrometry data for Lpp vs Lpp^{+21} was reanalyzed after extraction
600 from the whole cell proteomic data. Given the different tryptic peptides generated from the two isoforms of
601 Lpp, a shared peptide (red) was used to quantify the relative levels of each Lpp isoform in each of the strains.
602 The graphs document the relative levels of the peptide and show that the presence or absence of sorbitol in
603 the growth medium has no effect on the level of Lpp^{+21} relative to Lpp.

604

605 **Figure S3. Sub-cellular proteomics of Lpp^{+21} *E. coli*.** (A) Relative amount of protein in different subcellular
606 compartments, measured by the raw relative proportion of peptide intensities identified from proteins
607 annotated to reside in cellular compartments defined in the STEPdb. (B) Comparative proteome profile of the
608 wild-type and Lpp^{+21} strain for cell lysate and extracted outer membrane vesicles. Loading of each technical
609 replicate was normalized to OD_{600}. Representative data are shown from experiments performed in biological
610 triplicate.

611

612 **Figure S4. A synthetic lethal screen to determine genes essential to Lpp^{+21} *E. coli*.** An Hfr donor strain
613 carrying a selectable marker (*cat*) fused to *lpp*$^{+21}$, replacing the *lpp* ORF, is mated on agar plates with arrayed
614 F^- recipients (384) per plate carrying a selectable marker (*kan*) replacing other ORF. Upon mating, cells are
615 subjected the first round of selection (intermediate selection) using antibiotic kanamycin and then further
616 subjected to a second round of selection using both antibiotics; (A) depicts images of representative plates
617 generated in each step of the procedure with imaging and manual analysis step, cross-referencing of single
618 gene knock outs and double recombinants, included. (B) depiction of the strains as cartoons generated in each
619 step of the procedure. (C) A representative mini screen of manually selected genes from the main synthetic
620 lethal screen. Sterility controls were included on each mini screen. The mini screen was performed in 384-pin
621 density with each clone arrayed in four biological replicates, each having four technical replicates (blue
622 boxes). Synthetic lethal mutants identified from the mini screen were further verified by PCR to confirm the
623 presence of both gene modifications and rule out partial duplication events.

624

625 **Figure S5. Construction and characterization of the validation *yiaD* mutant.** A kanamycin resistance
626 cassette was amplified from pKD4 using primers with overhangs complementary to upstream and downstream

627 of *yiaD*. The PCR fragment was electroporated in BW25113 cells harbouring the λ –red recombineering
628 plasmid (pKD46). Transformants were selected on kanamycin-resistant plates and verified by PCR (methods).
629 Primers flanking the *yiaD* gene confirm replacement of *yiaD* with kanamycin cassette and primers amplifying
630 lpp confirm lpp^{+21} replacement of *lpp*. The sequence information for all primers used are included in Table
631 S5.
632
633 **Figure S6. Proteomics quality control report.** (A) Principle Component Analysis (PCA) plot of data from
634 triplicate samples of wild-type and Lpp^{+21} strains grown on M9 medium with or without supplementation by
635 sorbitol. (B) Sample Coefficient of variation plots for the same four samples.
636
637 **Figure S7. Molecular dynamics plots of Lpp tilt angles over time.** Plots of the angles over time, from
638 which the averages and standard deviations were derived. Simulation were run for 200 ns and average tilt
639 angles from the last 100 ns were calculated. To check for convergence, the Lpp simulation ran for an
640 additional 200 ns. The angle from the last 200 ns is 78.3 +/- 4.8°, nearly identical (within 1.4°) to that from
641 the 100-200 ns window.
642
643
644
645 **Table S1 Proteomic results**
646
647 **Table S2. Substantive changes in steady-state protein levels in cell envelope of Lpp^{+21}**
648
649 **Table S3: Proteins used in the generation of the sequence similarity network**
650
651 **Table S4: Representative Lpp protein information**
652
653 **Table S5: Bacterial strains and primers used in the study**
654
655 **Table S6: Genes up-regulated in Lpp+21 strain**
656

657 **REFERENCES**

658

659 1. Silhavy TJ, Kahne D, Walker S. The bacterial cell envelope. *Cold Spring Harb Perspect Biol* **2**,
660 a000414 (2010).

661

662 2. Gunasinghe SD*, et al.* The WD40 Protein BamB Mediates Coupling of BAM Complexes into
663 Assembly Precincts in the Bacterial Outer Membrane. *Cell Rep* **23**, 2782-2794 (2018).

664

665 3. Rassam P*, et al.* Supramolecular assemblies underpin turnover of outer membrane proteins in
666 bacteria. *Nature* **523**, 333-336 (2015).

667

668 4. Ursell TS, Trepagnier EH, Huang KC, Theriot JA. Analysis of surface protein expression reveals the
669 growth pattern of the gram-negative outer membrane. *PLoS Comput Biol* **8**, e1002680 (2012).

670

671 5. Freinkman E, Okuda S, Ruiz N, Kahne D. Regulated assembly of the transenvelope protein complex
672 required for lipopolysaccharide export. *Biochemistry* **51**, 4800-4806 (2012).

673

674 6. Sperandeo P, Martorana AM, Polissi A. The lipopolysaccharide transport (Lpt) machinery: A
675 nonconventional transporter for lipopolysaccharide assembly at the outer membrane of Gram-
676 negative bacteria. *J Biol Chem* **292**, 17981-17990 (2017).

677

678 7. Sperandeo P*, et al.* New insights into the Lpt machinery for lipopolysaccharide transport to the cell
679 surface: LptA-LptC interaction and LptA stability as sensors of a properly assembled transenvelope
680 complex. *J Bacteriol* **193**, 1042-1053 (2011).

681

682 8. Ekiert DC*, et al.* Architectures of Lipid Transport Systems for the Bacterial Outer Membrane. *Cell*
683 **169**, 273-285 e217 (2017).

684

685 9. Shrivastava R, Chng SS. Lipid trafficking across the Gram-negative cell envelope. *J Biol Chem* **294**,
686 14175-14184 (2019).

687

688 10. Pazos M, Peters K, Vollmer W. Robust peptidoglycan growth by dynamic and variable multi-protein
689 complexes. *Curr Opin Microbiol* **36**, 55-61 (2017).

690

691 11. Typas A, Banzhaf M, Gross CA, Vollmer W. From the regulation of peptidoglycan synthesis to
692 bacterial growth and morphology. *Nat Rev Microbiol* **10**, 123-136 (2011).

693

694 12. Paradis-Bleau C*, et al.* Lipoprotein cofactors located in the outer membrane activate bacterial cell
695 wall polymerases. *Cell* **143**, 1110-1120 (2010).

696

697 13. Typas A*, et al.* Regulation of peptidoglycan synthesis by outer-membrane proteins. *Cell* **143**, 1097-
698 1109 (2010).

699

14. Selkrig J*, et al.* Conserved features in TamA enable interaction with TamB to drive the activity of the translocation and assembly module. *Sci Rep* **5**, 12905 (2015).

15. Selkrig J*, et al.* Discovery of an archetypal protein transport system in bacterial outer membranes. *Nat Struct Mol Biol* **19**, 506-510, S501 (2012).

16. Shen HH*, et al.* Reconstitution of a nanomachine driving the assembly of proteins into bacterial outer membranes. *Nat Commun* **5**, 5078 (2014).

17. Cohen EJ, Ferreira JL, Ladinsky MS, Beeby M, Hughes KT. Nanoscale-length control of the flagellar driveshaft requires hitting the tethered outer membrane. *Science* **356**, 197-200 (2017).

18. Asmar AT*, et al.* Communication across the bacterial cell envelope depends on the size of the periplasm. *PLoS Biol* **15**, e2004303 (2017).

19. Baba T*, et al.* Construction of Escherichia coli K-12 in-frame, single-gene knockout mutants: the Keio collection. *Mol Syst Biol* **2**, 2006 0008 (2006).

20. Ingraham JL, Marr AG. Effects of temperature, pressure, pH, and osmotic stress on growth. In: *Escherichia coli and Salmonella: cellular and molecular biology* (eds Neidhardt FC*, et al.*). ASM Press (1996).

21. Stock JB, Rauch B, Roseman S. Periplasmic space in Salmonella typhimurium and Escherichia coli. *J Biol Chem* **252**, 7850-7861 (1977).

22. Cayley DS, Guttman HJ, Record MT, Jr. Biophysical characterization of changes in amounts and activity of Escherichia coli cell and compartment water and turgor pressure in response to osmotic stress. *Biophys J* **78**, 1748-1764 (2000).

23. Pilizota T, Shaevitz JW. Plasmolysis and cell shape depend on solute outer-membrane permeability during hyperosmotic shock in E. coli. *Biophys J* **104**, 2733-2742 (2013).

24. Domka J, Lee J, Bansal T, Wood TK. Temporal gene-expression in Escherichia coli K-12 biofilms. *Environ Microbiol* **9**, 332-346 (2007).

25. Mathelie-Guinlet M, Asmar AT, Collet JF, Dufrene YF. Lipoprotein Lpp regulates the mechanical properties of the E. coli cell envelope. *Nat Commun* **11**, 1789 (2020).

26. Li GW, Burkhardt D, Gross C, Weissman JS. Quantifying absolute protein synthesis rates reveals principles underlying allocation of cellular resources. *Cell* **157**, 624-635 (2014).

27. Loos MS*, et al.* Structural Basis of the Subcellular Topology Landscape of Escherichia coli. *Front Microbiol* **10**, 1670 (2019).

743
744 28. Sonntag I, Schwarz H, Hirota Y, Henning U. Cell envelope and shape of Escherichia coli: multiple
745 mutants missing the outer membrane lipoprotein and other major outer membrane proteins. *J*
746 *Bacteriol* **136**, 280-285 (1978).

747
748 29. Schwechheimer C, Kulp A, Kuehn MJ. Modulation of bacterial outer membrane vesicle production
749 by envelope structure and content. *BMC Microbiol* **14**, 324 (2014).

750
751 30. Rojas ER, Huang KC, Theriot JA. Homeostatic Cell Growth Is Accomplished Mechanically through
752 Membrane Tension Inhibition of Cell-Wall Synthesis. *Cell Syst* **5**, 578-590 e576 (2017).

753
754 31. Li H. Aligning sequence reads, clone sequences and assembly contigs with BWA-MEM. *ArXiv*
755 **1303**, (2013).

756
757 32. Xu Y*, et al.* Assembly and channel opening of outer membrane protein in tripartite drug efflux
758 pumps of Gram-negative bacteria. *J Biol Chem* **287**, 11740-11750 (2012).

759
760 33. Kim S, Yum S, Jo WS, Lee BL, Jeong MH, Ha NC. Expression and biochemical characterization of
761 the periplasmic domain of bacterial outer membrane porin TdeA. *J Microbiol Biotechnol* **18**, 845-
762 851 (2008).

763
764 34. Jo I, Kim JS, Xu Y, Hyun J, Lee K, Ha NC. Recent paradigm shift in the assembly of bacterial
765 tripartite efflux pumps and the type I secretion system. *J Microbiol* **57**, 185-194 (2019).

766
767 35. Shi X*, et al.* In situ structure and assembly of the multidrug efflux pump AcrAB-TolC. *Nat Commun*
768 **10**, 2635 (2019).

769
770 36. Gumbart JC*, et al.* Lpp positions peptidoglycan at the AcrA-TolC interface in the AcrAB-TolC
771 multidrug efflux pump. *Biophys J* **in press**, (2021).

772
773 37. Eklof JM, Tan TC, Divne C, Brumer H. The crystal structure of the outer membrane lipoprotein
774 YbhC from Escherichia coli sheds new light on the phylogeny of carbohydrate esterase family 8.
775 *Proteins* **76**, 1029-1036 (2009).

776
777 38. Bay DC, Stremick CA, Slipski CJ, Turner RJ. Secondary multidrug efflux pump mutants alter
778 Escherichia coli biofilm growth in the presence of cationic antimicrobial compounds. *Res Microbiol*
779 **168**, 208-221 (2017).

780
781 39. Shu W, Liu J, Ji H, Lu M. Core structure of the outer membrane lipoprotein from Escherichia coli at
782 1.9 A resolution. *J Mol Biol* **299**, 1101-1112 (2000).

783
784 40. Boags AT, Samsudin F, Khalid S. Binding from Both Sides: TolR and Full-Length OmpA Bind and
785 Maintain the Local Structure of the E. coli Cell Wall. *Structure* **27**, 713-724 e712 (2019).

786

787 41. Samsudin F, Boags A, Piggot TJ, Khalid S. Braun's Lipoprotein Facilitates OmpA Interaction with
788 the Escherichia coli Cell Wall. *Biophys J* **113**, 1496-1504 (2017).

789
790 42. Asmar AT, Collet JF. Lpp, the Braun lipoprotein, turns 50-major achievements and remaining issues.
791 *FEMS Microbiol Lett* **365**, (2018).

792
793 43. Inouye M, Shaw J, Shen C. The assembly of a structural lipoprotein in the envelope of Escherichia
794 coli. *J Biol Chem* **247**, 8154-8159 (1972).

795
796 44. Miller SI, Salama NR. The gram-negative bacterial periplasm: Size matters. *PLoS Biol* **16**, e2004935
797 (2018).

798
799 45. Babu M*, et al.* Quantitative genome-wide genetic interaction screens reveal global epistatic
800 relationships of protein complexes in Escherichia coli. *PLoS Genet* **10**, e1004120 (2014).

801
802 46. Babu M*, et al.* Genetic interaction maps in Escherichia coli reveal functional crosstalk among cell
803 envelope biogenesis pathways. *PLoS Genet* **7**, e1002377 (2011).

804
805 47. Tachikawa T, Kato J. Suppression of the temperature-sensitive mutation of the bamD gene required
806 for the assembly of outer membrane proteins by multicopy of the yiaD gene in Escherichia coli.
807 *Biosci Biotechnol Biochem* **75**, 162-164 (2011).

808
809 48. Ishida H, Garcia-Herrero A, Vogel HJ. The periplasmic domain of Escherichia coli outer membrane
810 protein A can undergo a localized temperature dependent structural transition. *Biochim Biophys Acta*
811 **1838**, 3014-3024 (2014).

812
813 49. Cho H*, et al.* Bacterial cell wall biogenesis is mediated by SEDS and PBP polymerase families
814 functioning semi-autonomously. *Nat Microbiol* **1**, 16172 (2016).

815
816 50. Mueller EA, Egan AJ, Breukink E, Vollmer W, Levin PA. Plasticity of Escherichia coli cell wall
817 metabolism promotes fitness and antibiotic resistance across environmental conditions. *Elife* **8**,
818 (2019).

819
820 51. Suzuki H, Nishimura Y, Hirota Y. On the process of cellular division in Escherichia coli: a series of
821 mutants of E. coli altered in the penicillin-binding proteins. *Proc Natl Acad Sci U S A* **75**, 664-668
822 (1978).

823
824 52. Chen ZY, Cao J, Xie L, Li XF, Yu ZH, Tong WY. Construction of leaky strains and extracellular
825 production of exogenous proteins in recombinant Escherichia coli. *Microb Biotechnol* **7**, 360-370
826 (2014).

827
828 53. Stohl EA, Lenz JD, Dillard JP, Seifert HS. The Gonococcal NlpD Protein Facilitates Cell Separation
829 by Activating Peptidoglycan Cleavage by AmiC. *J Bacteriol* **198**, 615-622 (2015).

830

54. Yang LC, Gan YL, Yang LY, Jiang BL, Tang JL. Peptidoglycan hydrolysis mediated by the amidase AmiC and its LytM activator NlpD is critical for cell separation and virulence in the phytopathogen Xanthomonas campestris. *Mol Plant Pathol* **19**, 1705-1718 (2018).

55. Rojas ER, Huang KC. Regulation of microbial growth by turgor pressure. *Curr Opin Microbiol* **42**, 62-70 (2018).

56. Hwang H, Paracini N, Parks JM, Lakey JH, Gumbart JC. Distribution of mechanical stress in the Escherichia coli cell envelope. *Biochim Biophys Acta Biomembr* **1860**, 2566-2575 (2018).

57. Rojas ER*, et al.* The outer membrane is an essential load-bearing element in Gram-negative bacteria. *Nature* **559**, 617-621 (2018).

58. Matias VR, Al-Amoudi A, Dubochet J, Beveridge TJ. Cryo-transmission electron microscopy of frozen-hydrated sections of Escherichia coli and Pseudomonas aeruginosa. *J Bacteriol* **185**, 6112-6118 (2003).

59. Jimenez Otero F, Chan CH, Bond DR. Identification of Different Putative Outer Membrane Electron Conduits Necessary for Fe(III) Citrate, Fe(III) Oxide, Mn(IV) Oxide, or Electrode Reduction by Geobacter sulfurreducens. *J Bacteriol* **200**, (2018).

60. Santos TC, Silva MA, Morgado L, Dantas JM, Salgueiro CA. Diving into the redox properties of Geobacter sulfurreducens cytochromes: a model for extracellular electron transfer. *Dalton Trans* **44**, 9335-9344 (2015).

61. Datsenko KA, Wanner BL. One-step inactivation of chromosomal genes in Escherichia coli K-12 using PCR products. *Proc Natl Acad Sci U S A* **97**, 6640-6645 (2000).

62. Gagarinova A, Babu M, Greenblatt J, Emili A. Mapping bacterial functional networks and pathways in Escherichia Coli using synthetic genetic arrays. *J Vis Exp*, (2012).

63. Deo P*, et al.* Outer membrane vesicles from Neisseria gonorrhoeae target PorB to mitochondria and induce apoptosis. *PLoS Pathog* **14**, e1006945 (2018).

64. Cox J, Mann M. MaxQuant enables high peptide identification rates, individualized p.p.b.-range mass accuracies and proteome-wide protein quantification. *Nat Biotechnol* **26**, 1367-1372 (2008).

65. Cox J, Neuhauser N, Michalski A, Scheltema RA, Olsen JV, Mann M. Andromeda: a peptide search engine integrated into the MaxQuant environment. *J Proteome Res* **10**, 1794-1805 (2011).

66. Shah AD, Goode RJA, Huang C, Powell DR, Schittenhelm RB. LFQ-Analyst: An Easy-To-Use Interactive Web Platform To Analyze and Visualize Label-Free Proteomics Data Preprocessed with MaxQuant. *J Proteome Res* **19**, 204-211 (2020).

875 67. Chen C, *et al.* Representative proteomes: a stable, scalable and unbiased proteome set for sequence
876 analysis and functional annotation. *PLoS One* **6**, e18910 (2011).

877
878 68. Gerlt JA, *et al.* Enzyme Function Initiative-Enzyme Similarity Tool (EFI-EST): A web tool for
879 generating protein sequence similarity networks. *Biochim Biophys Acta* **1854**, 1019-1037 (2015).

880
881 69. Shannon P, *et al.* Cytoscape: a software environment for integrated models of biomolecular
882 interaction networks. *Genome Res* **13**, 2498-2504 (2003).

883
884 70. Mitchell AL, *et al.* InterPro in 2019: improving coverage, classification and access to protein
885 sequence annotations. *Nucleic Acids Res* **47**, D351-D360 (2019).

886
887 71. Yamamoto N, *et al.* Update on the Keio collection of Escherichia coli single-gene deletion mutants.
888 *Mol Syst Biol* **5**, 335 (2009).

889
890 72. Yang J, Zhang Y. I-TASSER server: new development for protein structure and function predictions.
891 *Nucleic Acids Res* **43**, W174-W181 (2015).

892
893 73. Ortiz-Suarez ML, Samsudin F, Piggot TJ, Bond PJ, Khalid S. Full-Length OmpA: Structure,
894 Function, and Membrane Interactions Predicted by Molecular Dynamics Simulations. *Biophys J* **111**,
895 1692-1702 (2016).

896
897 74. Fiorin G, Klein ML, Hénin J. Using collective variables to drive molecular dynamics simulations.
898 *Mol Phys* **111**, 3345-3362 (2013).

899
900 75. Phillips JC, *et al.* Scalable molecular dynamics with NAMD. *J Comput Chem* **26**, 1781-1802 (2005).

901
902 76. Huang J, *et al.* CHARMM36m: an improved force field for folded and intrinsically disordered
903 proteins. *Nat Methods* **14**, 71-73 (2017).

904
905 77. Klauda JB, *et al.* Update of the CHARMM all-atom additive force field for lipids: validation on six
906 lipid types. *J Phys Chem B* **114**, 7830-7843 (2010).

907
908 78. Jorgensen WL, Chandrasekhar J, Madura JD, Impey RW, Klein ML. Comparison of simple potential
909 functions for simulating liquid water. *J Chem Phys* **79**, 926-935 (1983).

910
911 79. Darden TA, York DM, Pedersen LG. Particle mesh Ewald: An N log N method for Ewald sums in
912 large systems. *J Comput Phys* **98**, 10089-10092 (1993).

913
914 80. Balusek C, *et al.* Accelerating Membrane Simulations with Hydrogen Mass Repartitioning. *J Chem*
915 *Theory Comput* **15**, 4673-4686 (2019).

916

81. Humphrey W, Dalke A, Schulten K. VMD – Visual Molecular Dynamics. *J Mol Graphics* **14**, 33-38 (1996).